processes

MDPI

Article

Characteristics of Deformation and Stability of Ultra-Deep Pit in Plateau Alluvial–Lacustrine Gravel Strata

Yanhui Guo * and Shaoqian Liu

Faculty of Public Safety and Emergency Management, Kunming University of Science and Technology, Kunming 650093, China; liushaoqian0608@163.com
* Correspondence: guoyanhui0818@kust.edu.cn

Abstract: Deformation of ultra-deep pit walls and surrounding geotechnical bodies due to engineering disturbances typically shows intricate spatiotemporal patterns. In this study, deformations at critical steps of the construction process were first numerically simulated by Midas GTS NX, and this was followed by lab-scale geophysical model tests of the entire process of the pit construction. Data on deformation obtained from numerical simulations and lab-scale geophysical model tests were compared with those obtained from a dynamic monitoring scheme in the field to analyze the characteristics of the deformation and evolution of the pit wall. This was used to derive a generally applicable theoretical expression to predict variations in the horizontal displacements.

Keywords: ultra-deep pit; numerical simulation; lab-scale geophysical model test; dynamic monitoring in field; characteristics of evolution of deformation

Citation: Guo, Y.; Liu, S. Characteristics of Deformation and Stability of Ultra-Deep Pit in Plateau Alluvial–Lacustrine Gravel Strata. *Processes* **2024**, *12*, 941. https://doi.org/10.3390/pr12050941

Academic Editors: Carlos Sierra Fernández, Mahjoub Himi and Abbas Abbaszadeh Shahri

Received: 8 April 2024
Revised: 26 April 2024
Accepted: 29 April 2024
Published: 6 May 2024

1. Introduction

The continuing development of urban underground space requires the excavation of increasingly larger, deeper, and denser pits [1–3]. The excavation and support of a pit disturbs and changes the distribution of stress in the surrounding rock and soil mass and leads to the deformation, instability, and even failure of a pit with salient spatiotemporal characteristics [4,5]. Underground space engineering now involves the excavation of complex pits, such as ultra-large, ultra-deep pits, pit groups, and pits within pits. These emerging challenges not only deserve special attention from engineers but also require detailed investigation by researchers. Numerical simulations, lab-scale geophysical model tests, and dynamic monitoring in the field are commonly used to study the behavior of pits when they deform. These methods have different advantages and disadvantages. A pit is modeled in numerical simulations based on the observed parameters, but the anisotropy of the rock and soil masses, as well as their modes of connection, are idealized [6–8]. Lab-scale geophysical model tests avoid such simplification of the rock and soil masses, can be used to analyze trends and obtain other qualitative conclusions, and have a high reference value. However, such models can incur the effects of scale [9–11]. Data obtained from field monitoring are the most accurate of the three methods above but can be collected at only a limited number of measurement points, require a long time, and are expensive to obtain [12–15].

Numerous studies have investigated the disturbances and deformations caused by the construction of pits through the above-mentioned methods and have yielded important results. Cui et al. [16] analyzed monitoring data from a pit that had been excavated throughout the winter in a cold region and used them to investigate the deformation-related behavior of the pile wall and the causes of damage to it. Feng et al. [17] investigated the effects of the embedded depth and stiffness of a partition wall on lateral displacement and internal forces of the retaining structure and surrounding ground by using FE analysis and orthogonal experiments based on observation data on 20 pits that had been excavated for the construction of metro stations. Xu et al. [18] investigated the load on and the deformation of an ultra-deep (77.3 m) circular pit for a shield-receiving shaft at the Longquan Inverted Siphon section of the Central Yunnan Water Diversion Project by using monitoring data and found that the circular tube-shaped diaphragm wall deformed into an elliptical tube-shaped structure (stretched in one direction and compressed in the other). Shi et al. [19] separately simulated the stepwise and synchronous excavation of a large circular pit to explore lateral deformations of different sections of the retaining structure, the distribution of axial stress in the support, and the deformation of the surrounding ground. Yuan et al. [20] established a 2D coupled numerical model of drainage-induced consolidation during pit excavation and pit wall construction, discussed the use of numerical simulations and methods of modeling seepage in regional pits, and investigated the effects of the water-sealing curtain and the aquitard on horizontal displacement and settlement of ground surrounding pits.

After achieving certain progress in the field of pit deformation research using a single research method of on-site monitoring or numerical simulation, scholars began to lean towards using two different methods for more in-depth discussions and promoted lab-scale geophysical models. Massimino and Maugeri [21] analyzed the interaction between soil and foundation through two model experiments, recorded the time history of acceleration, and compared the results of the simulations and the model tests to assess the capability of the former for predicting the displacement and bearing capacity of the foundation. Hu et al. [22] analyzed the deformation-related behavior of pits under changing levels of confined water by conducting centrifugal model tests and numerical simulations and compared their results to investigate the effects of the length, depth, and area of the pit as well as the level of confined water in it on its three-dimensional (3D) spatial effects. Based on a large-scale (1:10) physical model test, Dou et al. [23] found that the data on the passive earth pressure obtained from the experiments were consistent with field observations in terms of both their magnitude and the trend of variations in them with the depth of excavation. Wang et al. [24] analyzed the deformation of a deep pit through on-site monitoring and numerical simulation and evaluated the stability of the pit with unsupported ribbed plate anchor support using the limit equilibrium method. However, the above studies on the deformation of pits have used only one or two of the three above-mentioned methods (numerical simulations, lab-scale geophysical model tests, and field monitoring). In addition, previous studies have focused on deformations in pits surrounded by several buildings that are unimportant compared to the main body of the pit [25–28].

The pits with complex characteristics of the evolution of deformation as well as spatiotemporal effects warrant multidimensional, multi-perspective investigation by combining several methods. In this study, the authors investigate the deformation of the top of pit walls and the ground surrounding the ultra-deep pit of Water Purification Plant No. 14 in Kunming City by using numerical simulations, lab-scale geophysical model tests, and on-site monitoring. The results provide references for the design and construction of rectangular pits, predictions of deformations in them, and the assessment of their stability.

2. Brief Description of the Pit

Water Purification Plant No. 14 in Kunming City was designed with an annual average production capacity of 260,000 m^3/d and serves a population of approximately 220,000 living in an area spanning 23.75 km^2. The main structures of the construction project included underground box structures and above-ground buildings. The underground box structures cover an area of 65,800 m^2. The retaining structure of the pit was 14–33 m deep and was divided into four sections that were separately constructed. This study investigated the room with a water intake pump in the first section of Kunming 14th Water Plant, which is a typical ultra-deep pit within a super large-scale pit. The pit was formed by removing 22,400 m^3 of earth and had a design depth of 33 m, a floor area of 32 (length) $\times$ 25 (width) m^2, edges with lengths of 114 m, and an area of 800 m^2. The retaining structure of the ultra-deep pit for the room with a water intake pump consisted of 1.2 m thick pit walls and steel bar-reinforced concrete supports. The pit walls consisted of 22 separate sections. The pit walls were 44 or 67 m high and 5.1–6.0 m wide. The steel bar cages were 44.25 or 68 m wide. Figure 1 shows the photos of the ultra-deep pit.

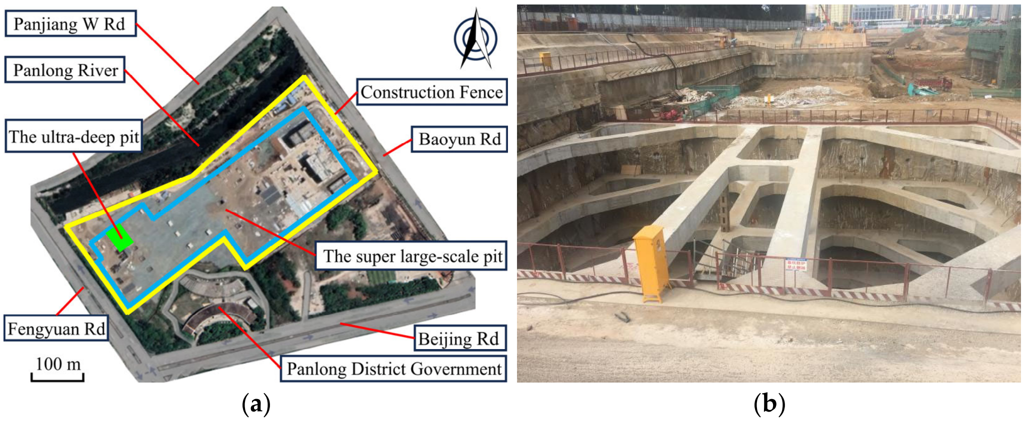

Figure 1. Photos of the ultra-deep pit: (**a**) the pit engineering plan and (**b**) the site photo of the pit walls and the internal supporting structures.

The pit is located in the northern region of Kunming City, in the central region of the Yunnan–Guizhou Plateau. Owing to the sedimentary environment of the lacustrine basin of the ancient Dian Lake and Panlong River, the construction ground consisted of a thick layer of gravelly soil with a high water content. Phreatic water was mainly found in the alluvial–diluvial gravelly soil strata from the Quaternary that were connected because there was no stably distributed aquiclude. The gravelly soil consisted of large, round particles and had a high water content and a high permeability. These properties posed several challenges to the construction of the pit, including the poor quality of the pile, easily collapsible holes, and inrushing water into the holes of the anchor cables. The excavation of the ultra-deep pit for the room with a water intake pump exposed the top five strata. The earthwork of the ultra-deep pit mainly involved the alluvial–lacustrine gravelly soil strata from the Quaternary (at an altitude of approximately 1981 m). Table 1 shows the mechanical parameters of the excavated strata, and Figure 2 shows the stratigraphic distribution map of the ultra-deep pit.

Table 1. Mechanical parameters of excavated strata.

No.	Soil Type	Unit Weight (kN/m^3)	Cohesion (kPa)	Internal Friction Angle (°)	Poisson's Ratio	Modulus of Elasticity (MPa)	Porosity
1	Backfill soil	18.7	19.5	8.5	0.28	7	0.94
2	Peat soil	13.2	20	6	0.40	12.1	2.16
3	Gravelly soil 1	19.4	10	22	0.31	240	-
4	Gravelly soil 2	19.4	10	21	0.31	240	-
5	Silty clay	19	40	12	0.30	16	0.84
6	Gravelly soil 3	19.4	10	22.5	0.31	240	-

The observed static water level in the proposed pit site is between 1.6 and 5.2 m, and the water level elevation is between 1899.03 and 1903.48 m. The water level in the whole site is high in the east and low in the west, and there is a certain slope drop in the groundwater surface. The ultra-deep pit of the water intake pump house is located on the west side of the site, with a depth of about 5.2 m at the infiltration line. Inside the ultra-deep pit of the water intake pump house, there are two 34 m deep dewatering wells, with the inner diameter of the steel pipe being 273 mm, and the pumping pipe in the wells is connected to the pumps with 100 mm fire belts. Three recharge wells are arranged along the west side of the pit wall to keep the groundwater level in a certain dynamic equilibrium state and prevent ground subsidence.

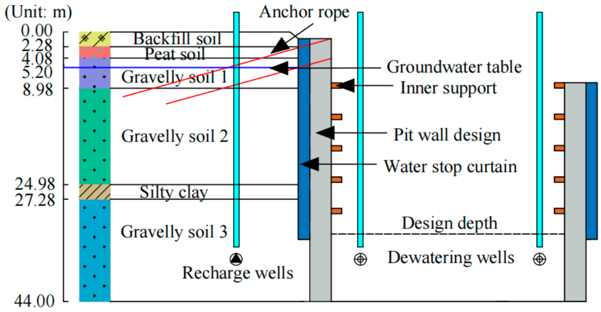

Figure 2. Stratigraphic distribution map of the ultra-deep pit.

3. Numerical Simulations of the Excavation and Support of Ultra-Deep Pit

Midas GTS NX was used to simulate the construction process of the ultra-deep pit based on the mechanical parameters of the major strata and the retaining and supporting structures. The ultra-deep pit was numerically simulated with a scale of 32 m × 25 m × 33 m in a coordinate system in which the positive directions of the X- and Y-axes corresponded to the north and west of the pit, respectively. For simulations to be as accurate as possible, the computational domain was extended beyond the prototype and had dimensions of 180 m × 120 m × 120 m. The pit walls and supports were strong and were simulated as linear elastic materials. The surrounding ground was assumed to be made of elastoplastic material satisfying the Mohr–Coulomb failure criterion. The model calculation adopts displacement boundary conditions, with fixed displacement in the x-direction at the left and right boundaries of the model, fixed displacement in the y-direction at the front and rear boundaries of the model, and fixed displacement in three directions at the bottom of the model. However, in order to make the numerical simulation results closer to the real deformation state, real mechanical parameters are used instead of local boundary conditions when modeling the pit wall (E: 31.5 GPa; μ: 0.3; γ: 26 kN/m^3). The overall numerical model of ultra-deep excavation includes 77,202 grids and 47,899 nodes, using a mixed grid consisting of hexahedral and tetrahedral grids. To achieve higher computational accuracy, the grid density near the pit wall is higher, and tetrahedral grids are used. The model of the pit was excavated in five layers, and five layers of support for it were constructed, with the excavation of each layer followed by the construction of support for it. Figure 3 shows the 3D numerical model of the ultra-deep pit. Figure 4 illustrates the simulated horizontal displacements of the pit at different time points during construction.

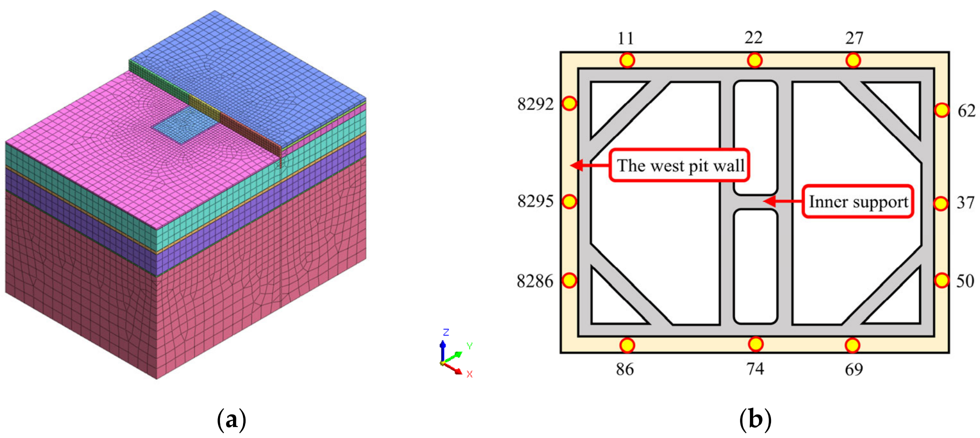

Figure 3. The 3D numerical model of the ultra-deep pit: (**a**) the numerical model and (**b**) the node positions in numerical models corresponding to monitoring points of lab-scale geophysical model tests and on-site.

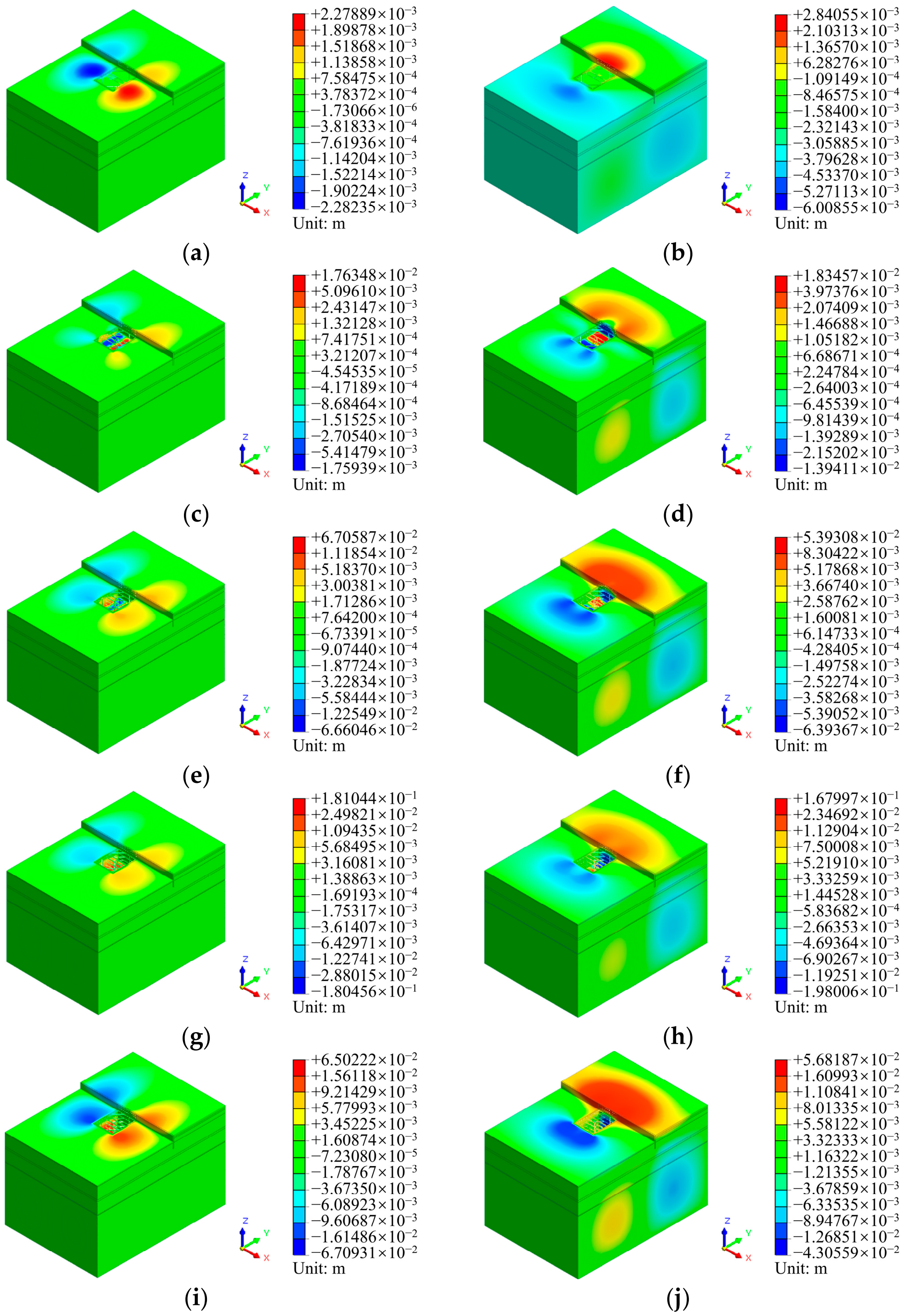

Figure 4. Numerically simulated horizontal displacements at different time points during construction: (**a**,**c**,**e**,**g**,**i**) the displacements along X-axis at time points #1, #2, #3, #4, and #5 and (**b**,**d**,**f**,**h**,**j**) the displacements along Y-axis at time points #1, #2, #3, #4, and #5.

The numerical simulations showed that once the ultra-deep pit had been excavated, the horizontal deformations of the top of pit walls and surrounding ground directed toward the pit exhibited significant spatiotemporal effects. The horizontal displacements were larger at positions closer to the pit. In addition, deformations were larger at positions closer to the edges of the rectangular pit, while those closer to the rectangular corners were smaller. As the corners of the pit have mutual support for the enclosure structures in both directions, the corner stiffness strengthening effect effectively limits the deformation at the right angles of the pit. The disturbed zones on the southern and northern sides were 32.77 m long on average, while those on the eastern and western sides were 50.39 m long on average. Figure 5 shows the horizontal displacements on each pit wall.

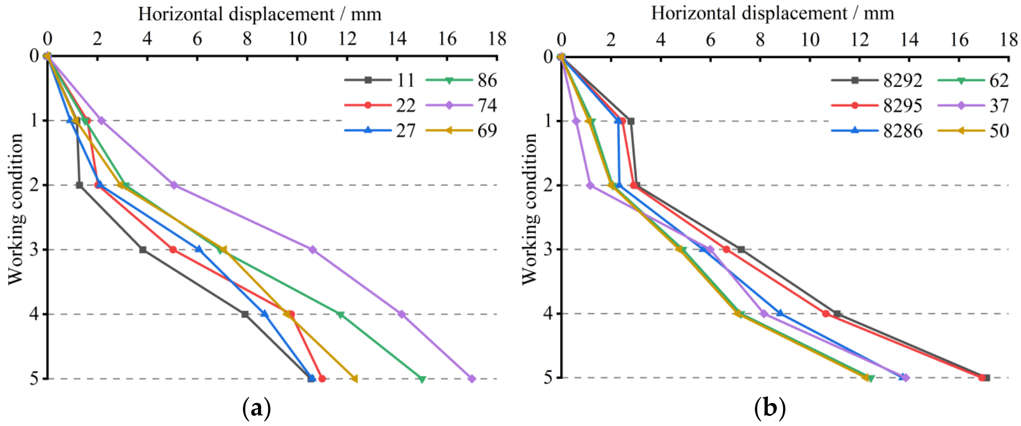

Figure 5. Horizontal displacements on each pit wall: (**a**) the southern and northern pit walls and (**b**) the western and eastern pit walls.

The horizontal displacements on the southern and northern pit walls exhibited similar temporal variations to those on the eastern and western pit walls, and the difference between the maximum lateral deformation on long-edged sides and that on short-edged sides was small. The maximum horizontal displacement at the top of the long-edged pit walls was approximately 17.9 mm, equal to approximately 0.0515% of the maximum depth of excavation of the pit. The maximum horizontal displacement at the top of the short-edged pit walls was approximately 17.1 mm, equal to approximately 0.0518% of the maximum depth of excavation of the pit.

4. Lab-Scale Geophysical Model Test of Ultra-Deep Pit in Gravelly Soil Strata

4.1. Monitoring and Testing Schemes

A laboratory model of the ultra-deep pit containing certain simplifications was built. The monitoring points were set up along the top of the pit walls, and the monitoring lines were established in the surrounding ground [29,30]. Accurately positioned marks were used to identify the monitoring points and lines as well as the reference points. White pins were used to identify the reference points, and red pins on a circular white background were used to identify monitoring points along the pit walls and monitoring lines in the surrounding ground.

A total of four reference points (RP-1 to RP-4 in Figure 6) were used and were located near the four corners of the rectangular pits but outside of the zones subject to disturbances from its excavation and construction. A total of 54 monitoring points were set up along the tops of the pit walls at a spacing of 2 cm, with 16 monitoring points each on the southern and the northern walls and 11 monitoring points each on the western and the eastern walls. A total of 174 horizontal monitoring points for displacement, arranged in 12 lines, were set up in the surrounding ground, with three lines with a spacing of 3 cm on each side. Figure 6 shows the configuration of monitoring items at the top of the pit walls.

Close-range photogrammetry technology uses images obtained from close-distance-target photography to determine the spatial positions of manual marking points [31–34]. A FUJIFILM-XT20 non-metric camera was used in the lab-scale geophysical model test to this end. The camera was mounted at a fixed position and took multiple photographs of the marks, which were subsequently used to measure changes in their 2D coordinates. Close-range photogrammetry spatial coordinate system with the east and north sides of the pit as positive X-axis and Y-axis directions, respectively, and the camera located in the positive Z-axis direction. Due to the distortion of the lens, the pixel coordinates of the images did not coincide with the actual pixel coordinates. Therefore, lens correction was performed on the images obtained by the camera by using the following equation in an image processing software (V.2021):

$$\begin{cases} x = x_u + \delta_x(x, y) \\ y = y_u + \delta_y(x, y) \end{cases} \tag{1}$$

where (x,y) are the pixel coordinates of the distorted image, (x_u,y_u) are the pixel coordinates of the actual scene, $\delta_x(x,y)$ is the distortion along the X-axis, and $\delta_y(x,y)$ is that along the Y-axis.

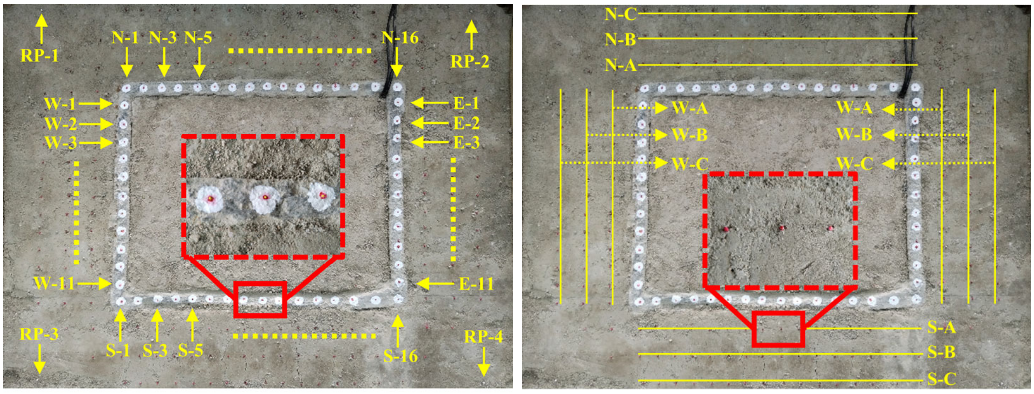

(**a**) (**b**)

Figure 6. Configuration of monitoring items at the top of pit walls: (**a**) the monitoring points and (**b**) the lines of monitoring points.

Following the correction of the close-range photographs, the 2D coordinates of the marks were calculated by using the single-station time-parallax method. A photograph of the target taken before it was deformed, referred to as the "zero photograph" here, was used to record the natural initial state of the target. Another photograph was taken after the target had been deformed. The on-site displacement of a monitoring point is obtained by scaling the displacement value generated on two photos of the monitoring point through the ratio of photography distance and camera main distance. The displacements of a characteristic point, Δx and Δz, were subsequently calculated as follows:

$$\begin{cases} \Delta_x = \Delta x_i \cdot z/f \\ \Delta_y = \Delta y_i \cdot z/f \end{cases} \tag{2}$$

where Δx and Δy are the actual displacements (m), Δx_i and Δy_i are the photographed displacements, viz. the parallax (mm), z is the distance (m) used for photography, and f is the principal distance.

Gravelly soil and similar materials were used as the filling materials of the model box. Based on similarity theory, the constant of geometric similarity was set to 100, the similarity ratios of the angle of internal friction and the unit weight were set to 1, and the modulus of compressibility and the similarity ratios of cohesion were set to 10. The mechanical parameters of the prototype were obtained by direct shear test and consolidation test and were compared with those of ideally similar materials [35–37]. Finally, the optimal mixing ratio of the material for simulating the water-rich gravelly strata was determined as follows: gypsum:liquid laundry detergent:bentonite:water:barite power:dolomitic sand = 1:1:1.4:3.5:8.8:13.2. The mixture was filled into the model box layer by layer. Liquid laundry detergent, the major active ingredient of which was a non-ionic surfactant, served to reduce water tension as well as regulate the cohesion of the mixture. The volume of the filling of the optimally similar material was 60 cm (length) × 50 cm (width) × 44 cm (height), and the mass of the filling was 292.83 kg.

The filled model was covered with a thin film and left to rest for 48 h. Once the entire volume of the fill material had settled and stabilized, the model was excavated. The excavation was performed in twenty steps over six stages (divided according to the five layers of support). The net depth of excavation in each step was 1.5–2 cm. Upon the completion of each step of excavation, the data on horizontal displacement were collected by using the close-range photogrammetry system. The depths (from the ground surface) of the five layers of internal support were −6, −14, −19, −24, and −29 cm. Figure 7 shows the preparation of the lab-scale geophysical model test of the ultra-deep pit, and Figure 8 shows the processes of excavation and support.

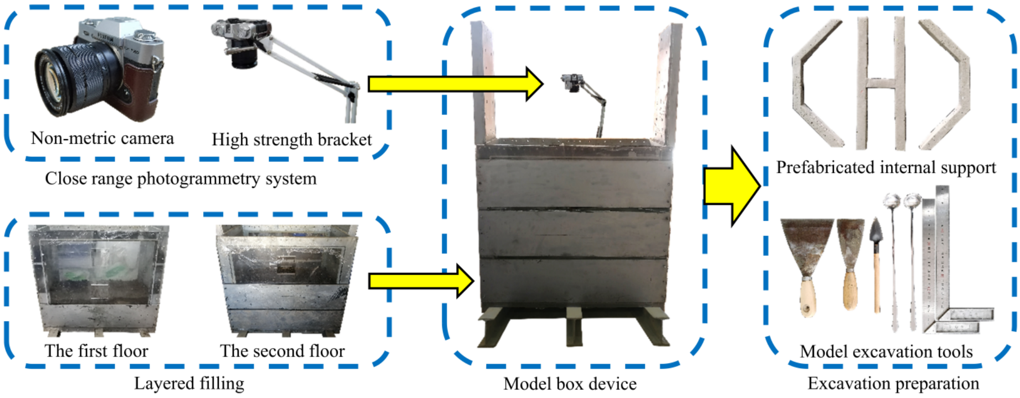

Figure 7. Preparation of the lab-scale geophysical model test of the ultra-deep pit.

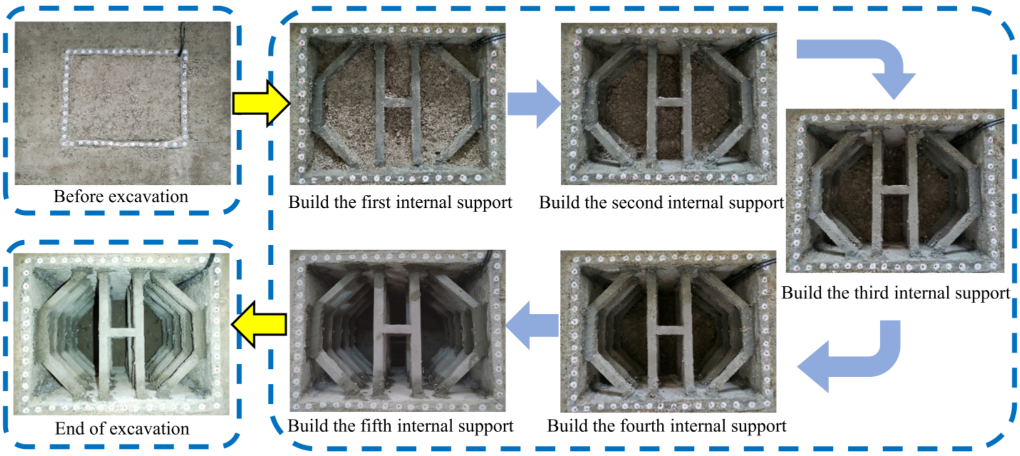

Figure 8. Excavation and support processes of the ultra-deep pit.

4.2. Analysis of Horizontal Displacement at the Top of Pit Walls

Excavation of soil inside pit walls disrupted the original equilibrium of stress and redistributed it; the pit walls and surrounding ground are horizontally displaced toward the pit as a result [38,39]. The pit walls were constrained by the internal supports to a certain degree. Consequently, the displacements at their top increased stepwise as excavation proceeded. The monitoring data on the horizontal displacements at the 54 measurement points along the pit walls were converted according to geometric similarity to obtain curves of the distribution of variations in the horizontal displacement with the depth of excavation. Figure 9 shows the horizontal displacements of the top of each pit wall obtained from the lab-scale geophysical model test.

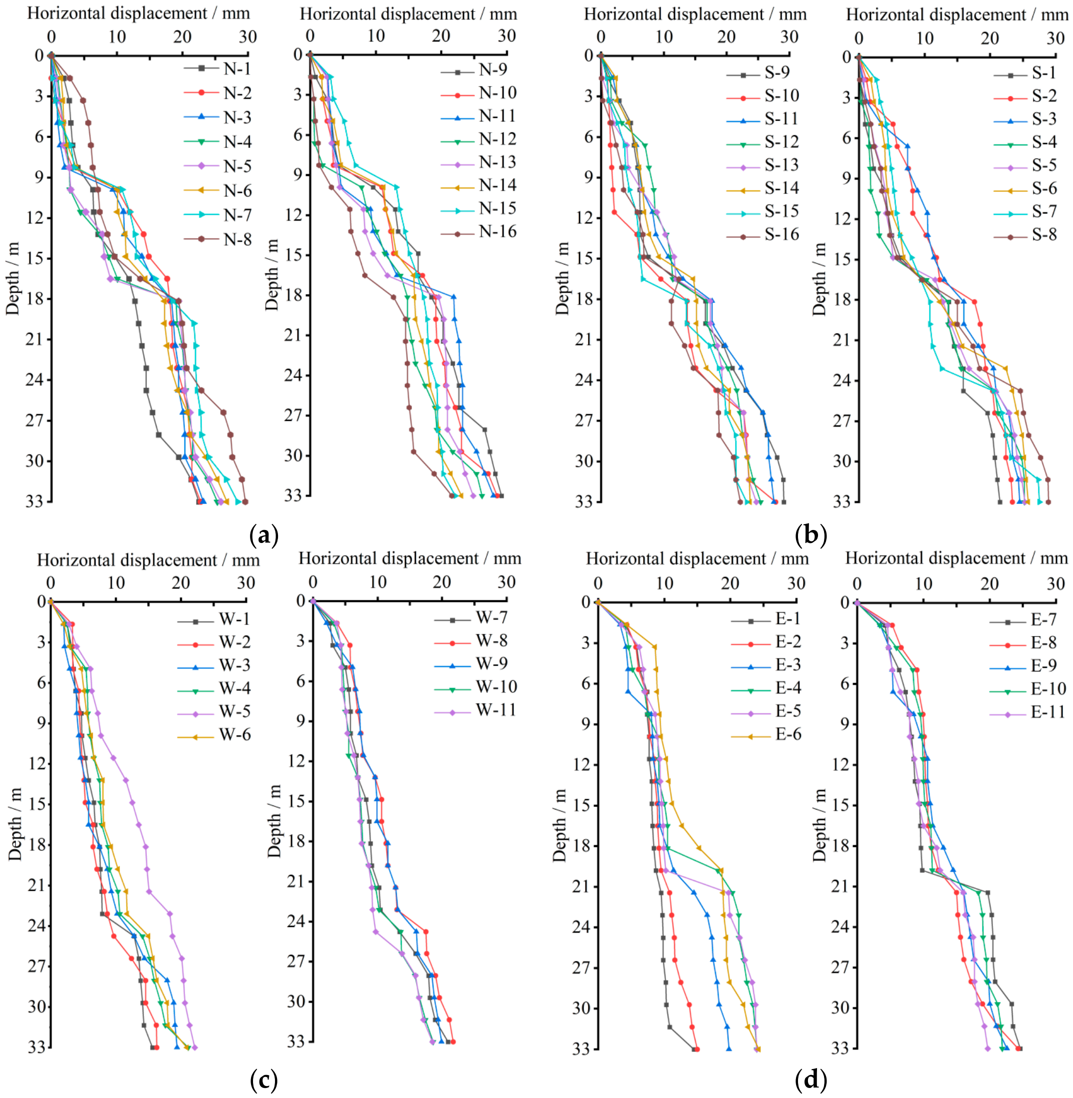

Figure 9. Horizontal displacements at the tops of each pit wall obtained from lab-scale geophysical model test: (**a**) the northern pit wall, (**b**) the southern pit wall, (**c**) the western pit wall, and (**d**) the eastern pit wall.

The horizontal displacements of the southern and northern pit walls exhibited similar trends. The eastern pit wall was more disturbed than the western pit wall by the construction of the third layer of supports at a depth of excavation of 19 m, resulting in drastic increases in the displacements at some monitoring points. Toward the end of the excavation, the incremental increases in the horizontal displacements at the tops of pit walls on all four sides decreased to varying degrees, with the displacements at most monitoring points increasing stably or stabilizing.

Once the excavation of the lab-scale geophysical model had been completed, the maximum horizontal deformation of the top of the northern pit wall was 29.16 mm (at monitoring point N-9), and the minimum deformation (at monitoring point N-16) was 74.07% of the maximum. The maximum horizontal displacement of the top of the southern pit wall was 29.10 mm (at monitoring point S-9), and the minimum deformation (at monitoring point S-1) was 73.88% of the maximum. The maximum and minimum horizontal displacements of the southern pit wall were consistent with those of the northern pit wall, with an average difference close to 1 mm. The maximum horizontal displacement of the top of the western pit wall was 22.1 mm (at monitoring point W-5), and the minimum deformation (at monitoring point W-1) was 70.59% of the maximum. The maximum horizontal deformation of the top of the eastern pit wall was 24.6 mm (monitoring point D-7). The difference between the maximum displacements of the eastern and western pit walls was 2.5 mm. The minimum deformation in the eastern pit wall was 58.94% of the maximum deformation.

4.3. Analysis of Cumulative Horizontal Displacements of the Surrounding Ground

Three lines of monitoring points were configured on each of the four sides of the model, with the line farthest from the pit, the line at the mean distance, and the line nearest to the pit designated as lines A, B, and C, respectively. The monitoring data were converted based on geometric similarity to establish graphs of the spatial distributions of cumulative displacements, which were consistent with those of the on-site prototype. Figure 10 shows the horizontal displacements of the ground on each side of the above model. The cumulative horizontal displacement of the surrounding ground had significant spatial effects, as did the horizontal displacements of the pit walls. As the distance between the ground and the pit increases, the total horizontal displacement decreases. Except for the western side, horizontal displacements at the central monitoring points were larger than those at monitoring points on the two sides in a line of monitoring points.

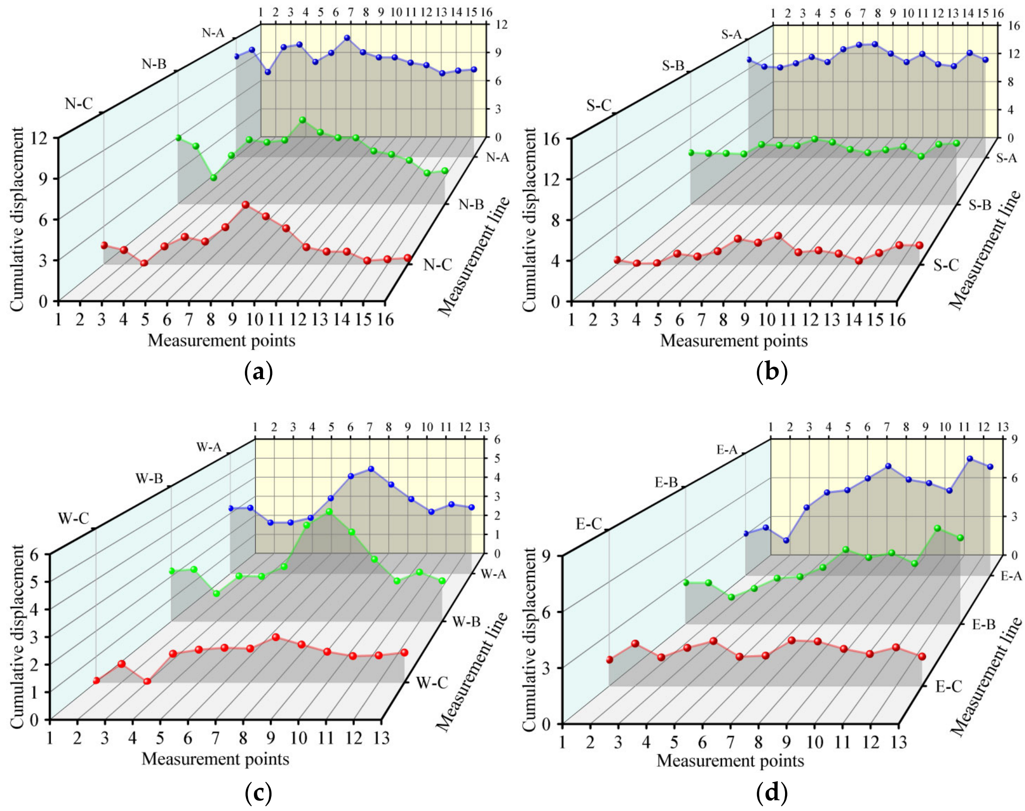

Figure 10. Horizontal displacements of the ground on each side of the model: (**a**) the northern side, (**b**) the southern side, (**c**) the western side, and (**d**) the eastern side.

The distance between the farthest lines of the monitoring points and the edges of the ultra-deep pit was approximately 10 m. The ratio of average displacements of the ground along the three lines of monitoring points on the northern side was N-A:N-B:N-C = 1:0.50:0.17, that along the three lines of monitoring points on the southern side was S-A:S-B:S-C = 1:0.50:0.10, the ratio between the average displacements of the ground along the three lines of monitoring points on the western side was W-A:W-B:W-C = 1:0.73:0.29, and that on the eastern side was E-A:E-B:E-C = 1:0.63:0.34. Based on these ratios of the model and the area of the disturbed surrounding ground obtained from the numerical simulations, the authors preliminarily estimated the range of disturbance in the surrounding ground due to the excavation of the ultra-deep pit and the support for it in gravelly soil strata to be 10–25 m on the southern and northern sides and 12–32 m on the eastern and western sides.

5. Evolution of Deformation of the Ultra-Deep Pit

5.1. Comprehensive Deformation Analysis Combined with On-Site Monitoring

Supporting structures that combine pit walls and internal supports are widely used to bolster pits as they can ensure their stability [40–44]. In response to earth pressure on the side of the pit being released, the pit walls are displaced laterally. The horizontal displacement at the tops of pit walls is a major index for measuring the safety of supporting structures of the pit and reflects the stability of the pit and the magnitude of the pressure of the earth behind the wall [45,46]. The authors designed a real-time systematic monitoring scheme involving setting measurement points along the top of the pit walls that were likely to undergo a large horizontal displacement. The resulting data were sorted and summarized. Figure 11 shows the on-site monitoring items at the top of the pit walls. Table 2 shows the corresponding relationships between the monitoring points used in the different methods. Figures 12–15 show a comparison of the horizontal displacements at the tops of pit walls obtained from the different methods.

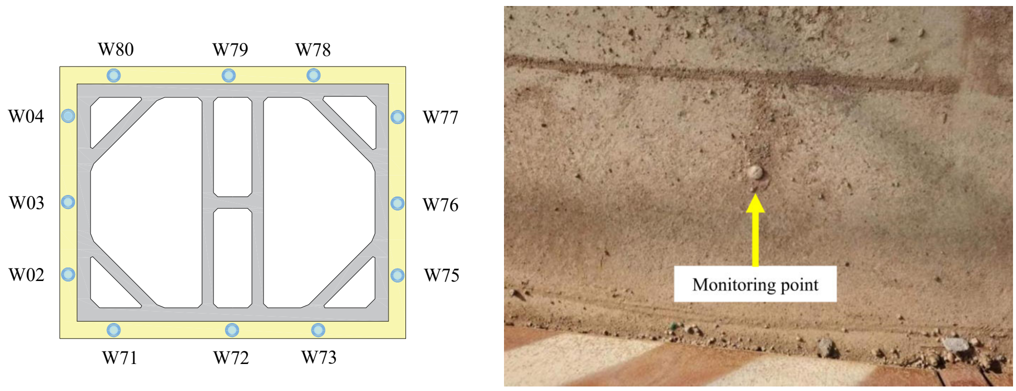

(**a**) (**b**)

Figure 11. On-site monitoring items at the top of pit walls: (**a**) on-site monitoring plan and (**b**) monitoring point.

Table 2. Corresponding relationships between monitoring points used in different methods.

Research Method	Serial Numbers of Monitoring Points					
On-site dynamic monitoring	WY71	WY72	WY73	WY78	WY79	WY80
Lab-scale geophysical model test	N-3	N-9	N-13	S-3	S-9	S-13
Node of numerical simulation	11	22	27	86	74	69
On-site dynamic monitoring	WY02	WY03	WY04	WY75	WY76	WY77
Lab-scale geophysical model test	W-10	W-6	W-2	E-10	E-6	E-2
Node of numerical simulation	8286	8295	8292	50	37	62

The data obtained from on-site dynamic monitoring and the lab-scale geophysical model test exhibited similar overall patterns of temporal variations. The horizontal displacement first increased, stabilized, and then increased again to exhibit an S-shaped trend of evolution. Numerical simulations showed first a slow increase and then a steady increase. The data from field monitoring showed that the horizontal displacement exhibited a stage of stable variation that was longer than that of the lab-scale geophysical model test and had a zero rate of variation. The horizontal displacements at temporal points #1 and #2 obtained from the numerical simulations differed considerably from those obtained from on-site dynamic monitoring and the lab-scale geophysical model test. Even though the lab-scale geophysical model test and the numerical simulations had appropriate parameters, the horizontal displacements obtained from the lab-scale geophysical model test were generally larger than those obtained from field monitoring, while those obtained from the numerical simulations were smaller than those obtained from field monitoring.

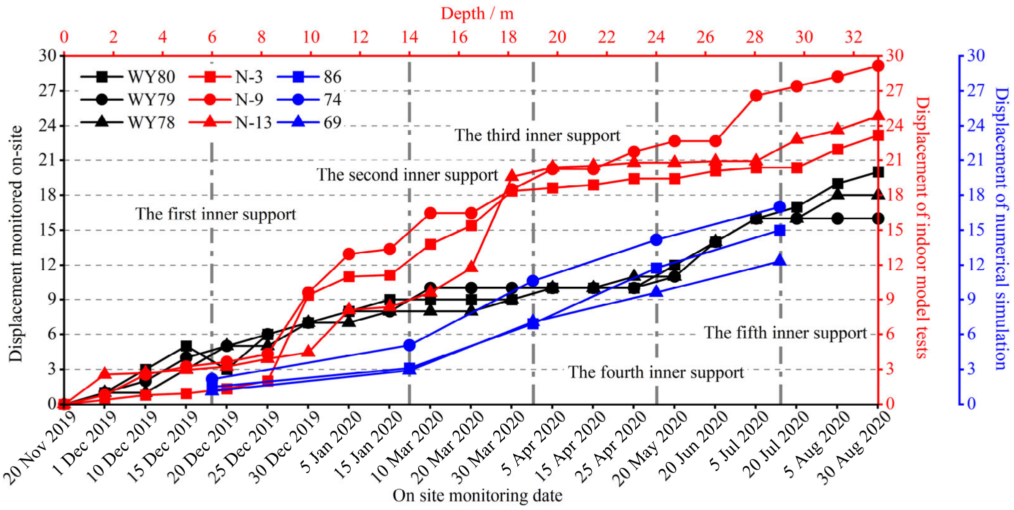

Figure 12. Comparison of horizontal displacements at the tops of northern pit wall.

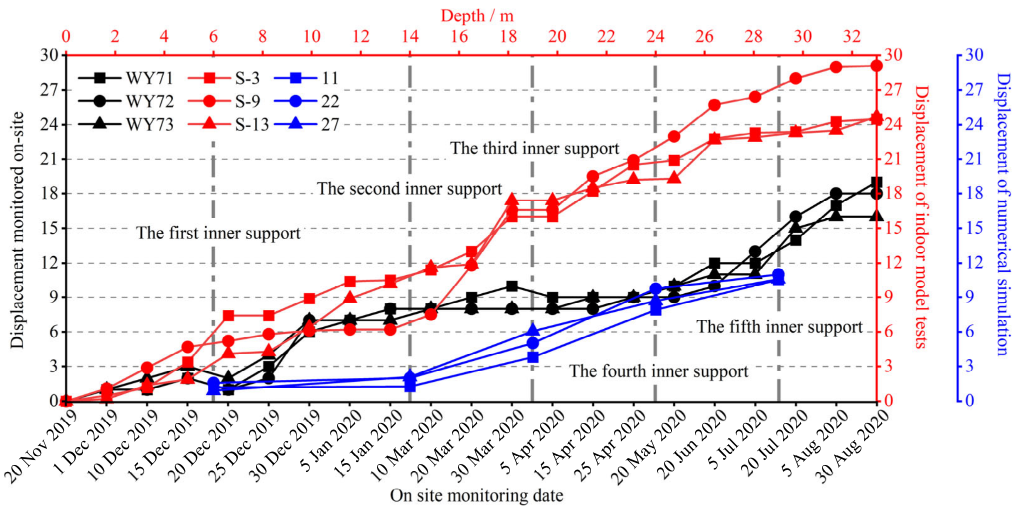

Figure 13. Comparison of horizontal displacements at the tops of southern pit wall.

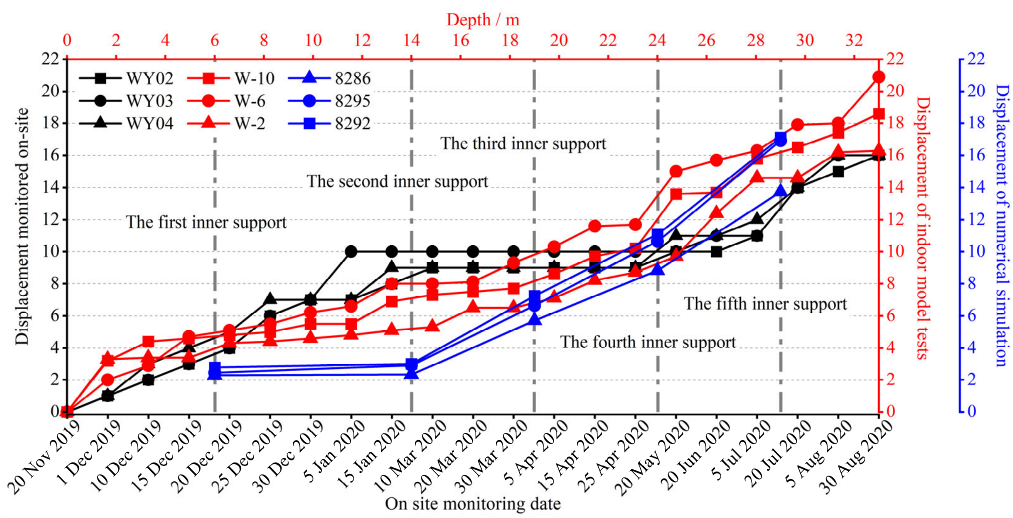

Figure 14. Comparison of horizontal displacements at the tops of western pit wall.

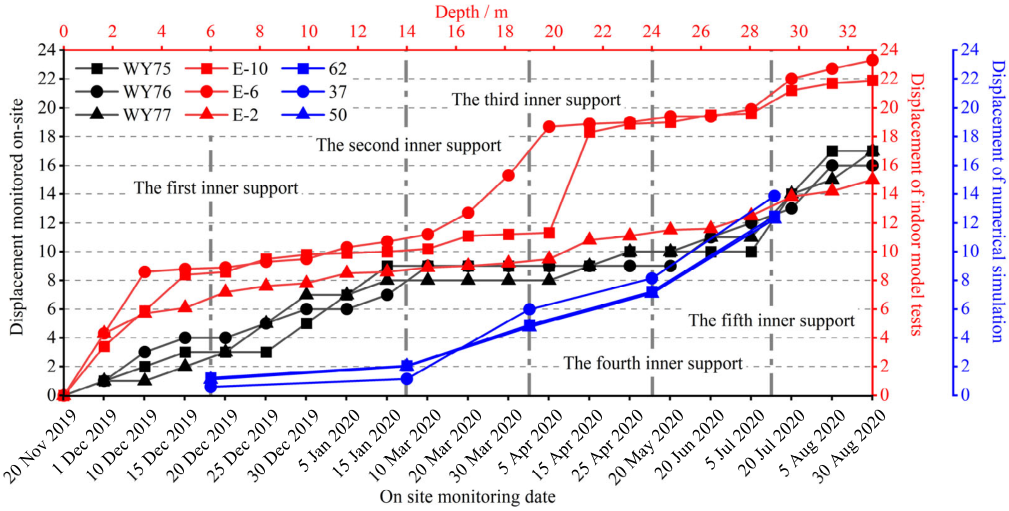

Figure 15. Comparison of horizontal displacements at the tops of eastern pit wall.

From the pit was excavated to the second internal support construction was completed, there was a difference in the horizontal displacement of the top of the pit walls. The average differences between the horizontal displacements obtained from dynamic monitoring and the lab-scale geophysical model test, those between dynamic monitoring and the numerical simulations, and between the latter and the lab-scale geophysical model test were 2.11, 3.91, and 5.109 mm, respectively. On the whole, the horizontal displacements at the tops of the pit walls, from the completion of the second layer of internal supports to the completion of the fifth layer of internal supports, obtained by using the three methods, exhibited large average incremental increases and similar trends of variation. This indicates that, during this period, the pit underwent significant disturbances due to excavation engineering. The omnidirectional average incremental increases obtained from the on-site dynamic monitoring, numerical simulations, and lab-scale geophysical model tests were 8.33, 11.07, and 12.52 mm, respectively.

Compared to the Coulomb theory, which focuses on wedges, the Rankine theory, which focuses on one point, is more suitable for the analysis of soil pressure on pit walls and roofs [47,48]. When conducting stress analysis, multiple strata should be considered as cohesive soil, and it should be noted that the drainage measures of the pit do not account for water pressure. The cohesive soil and internal support on both sides of the pit wall can respectively reduce and increase the σ_x of the stress Mohr circle, but the combined support structure of internal support and pit wall only provides horizontal stress in the ultimate equilibrium state and deformation. Therefore, when the pit wall undergoes vertical deformation, the cohesive soil generates active soil pressure with a soil pressure coefficient of K_a. However, when the pit wall is stable, this point may be in a limit equilibrium state. As excavation and support progress, the soil pressure at a certain point on the top of the pit wall is dynamically changing, and the soil pressure coefficient will fluctuate between K_0 and K_a.

5.2. Analysis and Prediction of the Stability of Retaining Structure

The authors compared the differences among the cumulative horizontal displacements at the tops of pit walls that were caused by the excavation of ultra-deep pit, at 12 field monitoring points, and at the corresponding nodes of the numerical simulations and the monitoring points of the lab-scale geophysical model test. Figure 16 shows the comparison of the cumulative displacements by using the three methods.

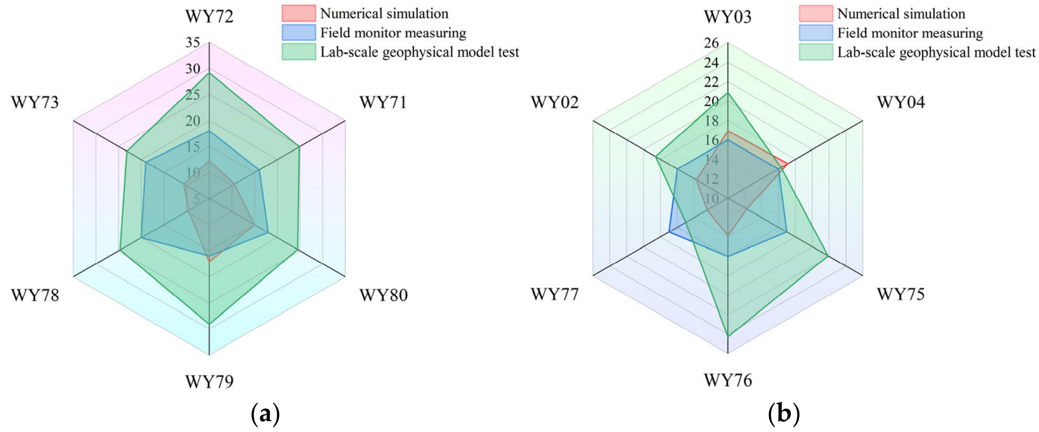

Figure 16. Comparisons of the cumulative displacements by using the three methods: (**a**) the southern and northern sides and (**b**) the western and eastern sides.

The maximum deformations observed through the above three methods were below the warning level, which shows that the design of the supporting structure based on a combination of pit walls and internal supports was appropriate and feasible. Considering that the spans of the southern and northern pit walls were larger than those of the eastern and western pit walls, the area of coverage representing the cumulative horizontal displacements in Figure 16a was larger than that in Figure 16b. The cumulative horizontal displacements at the tops of pit walls obtained using the three methods were different. The horizontal displacements obtained from the numerical simulations were the smallest; those obtained from the field monitoring were larger than them by 237.4%, and the horizontal displacements obtained from the lab-scale geophysical model test were larger than those yielded by the field monitoring and the numerical simulations by 242.4% and by 575.4%, respectively. These differences can be tentatively attributed to temporal effects. Excavation of the pit and installation of the support system were provided instantaneously during the numerical simulations. By contrast, these processes required time during the actual construction of the pit, and the retaining structure underwent slow deformation during this period. The different cumulative horizontal displacements obtained in the lab-scale geophysical model test were also related to temporal effects. The excavation in the model began before the internal supports were adequately consolidated and cured to achieve an equilibrium of stress.

Data on the displacement of pit walls obtained by using the three methods were divided into four groups corresponding to the four sides of the rectangular pit. They were then subjected to weighted averaging and linear regression analysis, and the results were used to predict the horizontal displacements at the tops of pit walls based on sigmoid functions. The predicted horizontal displacements at the tops of the pit walls of the rectangular (length-to-width ratio = 1.28) ultra-deep pit increased monotonically but non-uniformly as the depth of excavation increased. The trends of the sigmoid function on the short-edged sides were more typical than those on the long-edged sides. For the design, construction, and prediction of deformations of retaining structures for pits, this empirical formula and its parametric ranges will be helpful. Figure 17 shows the sigmoid functions for predicting the horizontal displacements at the tops of pit walls on each side.

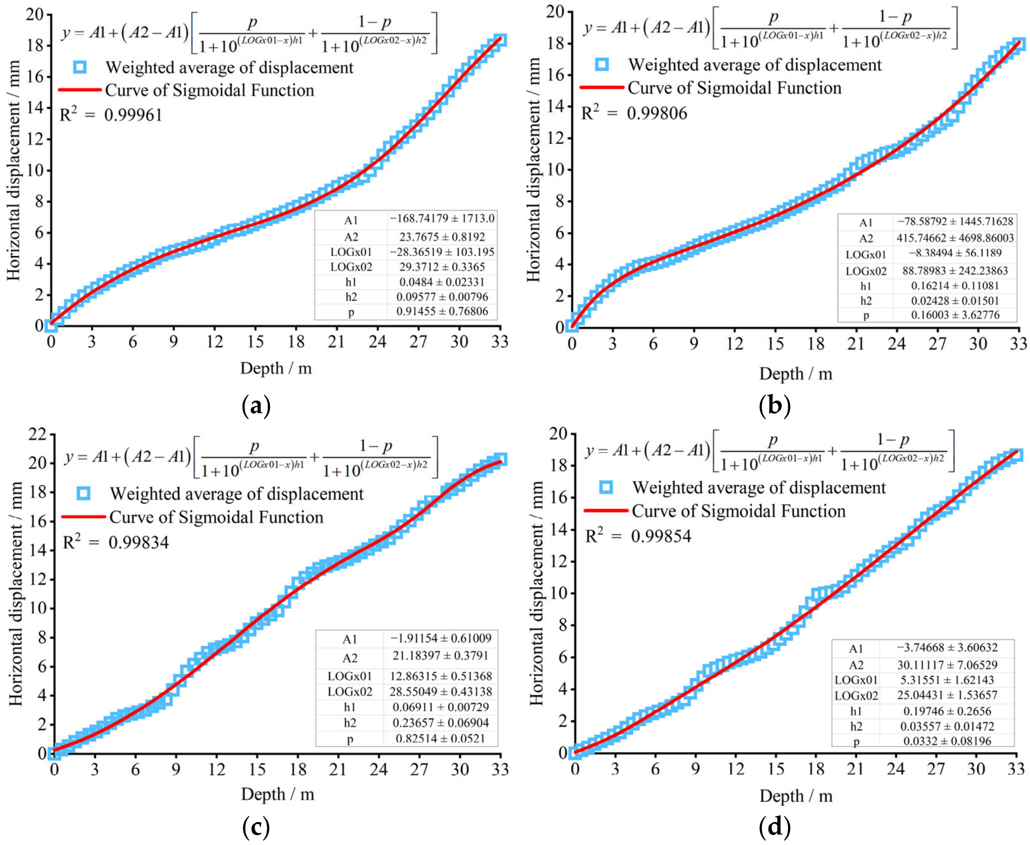

Figure 17. Sigmoid functions for predicting horizontal displacements at the tops of pit walls: (**a**) the western pit wall, (**b**) the eastern pit wall, (**c**) the northern pit wall, and (**d**) the southern pit wall.

6. Conclusions

Compared to previous studies, this study used more research methods to have a deeper discussion on the deformation of ultra-deep pits. The horizontal displacements of the pit wall and the surrounding ground were investigated by field parametric numerical simulations and lab-scale geophysical model tests based on close-up photogrammetry, revealing significant spatial and temporal effects during excavation and support. Then, the horizontal displacements of the pit wall obtained using different methods were compared and predicted by regression with a sigmoid function:

(1) The horizontal displacement of surrounding ground in numerical simulation increased with the distance from the pit, while soil masses near the four corners of the pit had higher rigidity and underwent smaller displacements. The horizontal displacements on the southern and northern pit walls exhibited similar trends of temporal variations to those of the eastern and western pit walls, and the difference between the maximum lateral deformation on long-edged sides and that on short-edged sides was small.

(2) The horizontal displacements of the southern and northern pit walls in lab-scale geophysical model tests exhibited similar trends. The eastern pit wall was more disturbed than the western pit wall by the construction of the third layer of supports at a depth of excavation of 19 m, resulting in drastic increases in displacements at some monitoring points. The maximum horizontal displacements at the tops of northern, southern, western, and eastern pit walls were 29.16, 29.10, 22.10, and 24.60 mm, respectively. Based on the results of lab-scale geophysical model tests and numerical simulations, the authors preliminarily estimated the range of disturbances in the ground surrounding the excavated ultra-deep pit and its supports in the gravelly soil strata to be 10–25 m on the southern and northern sides and 12–32 m on the eastern and western sides.

(3) The data obtained from on-site dynamic monitoring and the lab-scale geophysical model test exhibited similar overall patterns of temporal variations. The horizontal displacement first increased, stabilized, and then increased again to exhibit an S-shaped trend of evolution. According to data from the numerical simulations, it exhibited a trend of first increasing slowly and then increasing stably. The overall displacements at the tops of the pit walls obtained by using the three methods differed owing to temporal effects. The displacements obtained from the lab-scale geophysical model test were the largest, followed by those obtained from the on-site monitoring and the numerical simulations. The predicted horizontal displacements at upper sections of the pit walls of rectangular (length-to-width ratio = 1.28) ultra-deep pit increased monotonically but non-uniformly as the depth of excavation increased. The sigmoidal trends on the short-edged sides were more typical than those on the long-edged sides.

Due to the idealized geological distribution in numerical simulations and the uncertainty caused by size effects in lab-scale geophysical model tests, there are certain differences in the deformation characteristics obtained by different research methods. However, the research findings in this article will provide a research basis for narrowing this difference and using limit equilibrium theory to further discuss deformation characteristics. In addition, this ultra-deep pit has a high original groundwater table and has systematic drainage measures. According to unsaturated soil mechanics and previous studies [49–52], groundwater and unsaturated zones above the saturation zone may play a crucial role in the stability of pit walls. Discussing the effect of soil on the pit wall after dewatering will be a very valuable research direction for the next phase of this study.

Author Contributions: Conceptualization, Y.G.; methodology, Y.G.; software, Y.G. and S.L.; validation, Y.G. and S.L.; formal analysis, Y.G. and S.L.; investigation, Y.G. and S.L.; resources, Y.G. and S.L.; writing—original draft preparation, Y.G. and S.L.; funding acquisition, Y.G. All authors have read and agreed to the published version of the manuscript.

Funding: This work was supported by the following research funds: the General Projects of Yunnan Fundamental Research Projects (No. 202301AT070454); the Talent Training Fund of Kunming University of Science and Technology (No. KKZ3202367014); the "Xingdian Talent Support Plan of Yunnan Province" project; the National Innovation and Entrepreneurship Training Project for College Students of China (Nos. 2021106740085 and 2021106740086); the Key Technology Research and Pilot Test of Underground Coal Gasification, a major scientific and technological research project of the CNPC (No. 2019E-25); the Scientific Research Fund Project of Yunnan Provincial Department of Education, China (No. 2022J0065); and the Key Projects of Analysis and Testing Fund of Kunming University of Science and Technology, China (No. 2021T20200145).

Data Availability Statement: All relevant data are within this paper.

Conflicts of Interest: The authors declare no conflicts of interest.

References

1. Bobylev, N. Mainstreaming sustainable development into a city's Master plan: A case of Urban Underground Space use. *Land Use Policy* **2009**, *26*, 1128–1137. [CrossRef]
2. Qian, Q.H. Challenges Faced by Underground Projects Construction Safety and Countermeasures. *Chin. J. Geotech. Eng.* **2012**, *31*, 1945–1956.
3. Otake, Y.; Honjo, Y. Challenges in geotechnical design revealed by reliability assessment: Review and future perspectives. *Soils Found* **2022**, *62*, 101129. [CrossRef]
4. Einav, I. Soil mechanics: Breaking ground. *Philos. Trans. R. Soc. A* **2007**, *365*, 2985–3002. [CrossRef]
5. Westermann, K.; Meier, J.; Pitteloud, L. Excavation pit and foundation of a research center. *Bautechnik* **2020**, *97*, 878–885. [CrossRef]
6. Gotman, A.L.; Gotman, Y.A. Numerical Analysis of the Shorings of Deep Foundation Pits with Regard for the Soil Solidification. *Soil Mech. Found Eng.* **2019**, *56*, 225–231. [CrossRef]
7. Zhu, G.J.; Yu, S.Y.; Ning, Y.; Ren, X.H.; Wei, P.; Wu, Y. Numerical Simulation on the Progressive Failure Processes of Foundation Pit Excavation Based on a New Particle Failure Method. *Geofluids* **2021**, *2021*, 7374363. [CrossRef]
8. Zhao, C.; Feng, Y.; Wang, W.J.; Niu, Z.J. Mechanical Properties and Numerical Analysis of Underground Continuous Wall in Underground Grain Silo Foundation Pit. *Buildings* **2023**, *13*, 293. [CrossRef]

9. Liang, F.Y.; Chu, F.; Song, Z.; Li, Y.S. Centrifugal model test research on deformation behaviors of deep foundation pit adjacent to metro stations. *Rock Soil Mech.* **2012**, *33*, 657–664.
10. Fan, Q.Y.; Chen, B.; Shen, B. Model test research of bolt supporting of foundation pit considering construction process. *Rock Soil Mech.* **2005**, *26*, 1874–1878.
11. Guo, Y.H.; Kong, Z.J.; He, J.; Yan, M. Development and Application of the 3D Model Test System for Water and Mud Inrush of Water-Rich Fault Fracture Zone in Deep Tunnels. *Math. Probl. Eng.* **2021**, *2021*, 8549094. [CrossRef]
12. Liu, P.; Xie, S.L.; Zhou, G.Y.; Zhang, L.X.; Zhang, G.X.; Zhao, X.F. Horizontal displacement monitoring method of deep foundation pit based on laser image recognition technology. *Rev. Sci. Instrum.* **2018**, *89*, 125006. [CrossRef] [PubMed]
13. Yin, H.; Zhang, H.; Zhang, R. Measurement and Simulation Analysis of Vertical Cross Longitudinal Settlement between Turning Shield and Foundation Pit. *Adv. Civ. Eng.* **2021**, *2021*, 6698268. [CrossRef]
14. Lin, P.; Liu, P.; Ankit, G.; Singh, Y.J. Deformation Monitoring Analysis and Numerical Simulation in a Deep Foundation Pit. *Soil Mech. Found. Eng.* **2021**, *58*, 56–62. [CrossRef]
15. Zhao, J.P.; Tan, Z.S.; Yu, R.S.; Li, Z.L.; Zhang, X.R.; Zhu, P.C. Deformation responses of the foundation pit construction of the urban metro station: A case study in Xiamen. *Tunn. Undergr. Sp. Tech.* **2022**, *128*, 104662. [CrossRef]
16. Cui, G.H.; Liu, S.H.; Wang, Z.L. Excavation monitoring of a pile anchor support deep pit in Harbin. *J. Build. Struct.* **2016**, *37*, 144–150.
17. Feng, C.L.; Zhang, D.L.; Fang, Q.; Hou, Y.J. Research on diaphragm wall mechanism and effect of deformation control in soft soil. *Chin. J. Geotech. Eng.* **2018**, *40*, 2087–2095.
18. Xu, Q.W.; Gong, Z.Y.; Sun, Z.L.; Hu, R.C.; Hu, K.F. Analysis on the monitoring results of construction deformation and internal force of ultra-deep circular foundation pit of Dianzhong Water Diversion Project. *China Civ. Eng. J.* **2022**, *55*, 102–111.
19. Shi, H.; Jia, Z.L.; Wang, T.; Cheng, Z.Q.; Zhang, D.; Bai, M.Z.; Yu, K. Deformation Characteristics and Optimization Design for Large-Scale Deep and Circular Foundation Pit Partitioned Excavation in a Complex Environment. *Buildings* **2022**, *12*, 1292. [CrossRef]
20. Yuan, C.F.; Hu, Z.H.; Zhu, Z.; Yuan, Z.J.; Fan, Y.X.; Guan, H.; Li, L. Numerical Simulation of Seepage and Deformation in Excavation of a Deep Foundation Pit under Water-Rich Fractured Intrusive Rock. *Geofluids* **2021**, *2021*, 6628882. [CrossRef]
21. Massimino, M.R.; Maugeri, M. Physical modelling of shaking table tests on dynamic soil-foundation interaction and numerical and analytical simulation. *Soil Dyn. Earthq. Eng.* **2013**, *49*, 1–18. [CrossRef]
22. Hu, Y.; Li, Y.A.; Li, B.; Li, C.A.; Xiao, J.F. Centrifugal model tests and numerical simulation of three-dimensional space effect of deep and large foundation pit under the confined water level fluctuation. *Rock Soil Mech* **2018**, *39*, 1999–2007.
23. Dou, B.Y.; Zhang, J.P.; Yang, Y.C.; Niu, X.C. Study on Soil Deformation Parameters Around Deep Pit by Large-Scale Physical Model Test. *J. Basic Sci. Eng.* **2019**, *27*, 216–225.
24. Wang, Z.L. Numerical analysis of deformation control of deep foundation pit in Ulanqab city. *Geotech. Geol. Eng.* **2021**, *39*, 5325–5337. [CrossRef]
25. Mangushev, R.A.; Osokin, A.I.; Garnyk, L.V. Experience in Preserving Adjacent Buildings During Excavation of Large Foundation Pits Under Conditions of Dense Development. *Soil Mech. Found. Eng.* **2016**, *53*, 291–297. [CrossRef]
26. Ahmad, I.; Tayyab, M.; Zaman, M.; Anjum, M.N.; Dong, X.H. Finite-Difference Numerical Simulation of Dewatering System in a Large Deep Foundation Pit at Taunsa Barrage, Pakistan. *Sustainability* **2019**, *11*, 694. [CrossRef]
27. Liu, B.; Lin, H.; Chen, Y.; Liu, J.; Guo, C. Deformation Stability Response of Adjacent Subway Tunnels considering Excavation and Support of Foundation Pit. *Lithosphere* **2022**, *2022*, 7227330. [CrossRef]
28. Diao, H.G.; Tian, Y.; Wei, G.; Wang, X.Q.; Li, X. Multi-Effects of Tunneling and Basement Excavation on Existing Pile Group. *Symmetry* **2022**, *14*, 1928. [CrossRef]
29. Zhu, C.; Yan, Z.H.; Lin, Y.; Xiong, F.; Tao, Z.G. Design and Application of a Monitoring System for a Deep Railway Foundation Pit Project. *IEEE Access* **2019**, *7*, 107591–107601. [CrossRef]
30. Meng, L.Y.; Zou, J.G.; Liu, G.J. Research on the Design and Automatic Recognition Algorithm of Subsidence Marks for Close-Range Photogrammetry. *Sensors* **2020**, *20*, 544. [CrossRef]
31. Jiang, R.; Jauregui, D.V.; White, K.R. Close-range photogrammetry applications in bridge measurement: Literature review. *Measurement* **2008**, *41*, 823–834. [CrossRef]
32. Ngeljaratan, L.; Moustafa, M.A. Implementation and Evaluation of Vision-Based Sensor Image Compression for Close-Range Photogrammetry and Structural Health Monitoring. *Sensors* **2020**, *20*, 6844. [CrossRef] [PubMed]
33. Ngeljaratan, L.; Moustafa, M.A. Underexposed Vision-Based Sensors Image Enhancement for Feature Identification in Close-Range Photogrammetry and Structural Health Monitoring. *Appl. Sci.* **2021**, *11*, 11086. [CrossRef]
34. Li, X.; Li, W.; Yuan, X.A.; Yin, X.K.; Ma, X. DoF-Dependent and Equal-Partition Based Lens Distortion Modeling and Calibration Method for Close-Range Photogrammetry. *Sensors* **2020**, *20*, 5934. [CrossRef] [PubMed]
35. Park, S.Y.; Lee, S.W. A study on the establishment of similarity rule for tunneling model tests. *J. Korean Tunn. Undergr. Sp. Assoc.* **2004**, *6*, 161–170.
36. Gendarz, P. Technical means series of types generation process with constructional similarity theory use. *Forsch Ingenieurwes* **2013**, *77*, 105–115. [CrossRef]
37. Guo, Y.H.; Yang, Y.; Kong, Z.J.; He, J. Development of similar materials for liquid-solid coupling and its application in water outburst and mud outburst model test of deep tunnel. *Geofluids* **2022**, *2022*, 8784398. [CrossRef]

38. Min, Y.; Zhang, J.F.; Wang, R.X. Analysis of internal force of deformation of retaining wall in pits-in-pits. *Rock Soil Mech.* **2016**, *37*, 3270–3274.
39. Xu, C.J.; Cheng, S.Z.; Cai, Y.Q.; Luo, Z.Y. Deformation characteristic analysis of foundation pit under asymmetric excavation condition. *Rock Soil Mech.* **2014**, *35*, 1929–1934.
40. Peric, L. Foundation pit protection by shotcrete wall and ground anchors. *Gradevinar* **2008**, *60*, 1–11.
41. Shi, Y.F.; Yang, J.S.; Bai, W.; Zhang, X.M. Analysis of Field Testing for Deformation and Internal Force Of Unsymmetrical Loaded Foundation Pit'S Enclosure Structure Close To Railway. *Chin. J. Rock Mech. Eng.* **2011**, *30*, 826–833.
42. Zeng, C.F.; Xue, X.L.; Li, M.K. Use of cross wall to restrict enclosure movement during dewatering inside a metro pit before soil excavation. *Tunn. Undergr. Sp. Tech.* **2021**, *112*, 103909. [CrossRef]
43. Ter-Martirosyan, Z.G.; Ter-Martirosyan, A.Z.; Vanina, Y.V. Mathematical Computations of Long-Term Settlement and Bearing Capacity of Soil Bases and Foundations near Vertical Excavation Pits. *Axioms* **2022**, *11*, 679. [CrossRef]
44. Wang, X.Y.; Song, Q.Y.; Gong, H. Research on Deformation Law of Deep Foundation Pit of Station in Core Region of Saturated Soft Loess Based on Monitoring. *Adv. Civ. Eng.* **2022**, *2022*, 7848152. [CrossRef]
45. Yin, H.; Wang, S.; Wang, D.; Dong, Z.; Gao, Z.; Zhang, Z. Sheltering effect induced by established station to the new station excavation in Zhengzhou. *Arch. Civ. Mech. Eng.* **2023**, *23*, 175. [CrossRef]
46. Han, M.; Chen, X.; Jia, J. Analytical solution for displacement-dependent 3D earth pressure on flexible walls of foundation pits in layered cohesive soil. *Acta Geotech.* **2024**. [CrossRef]
47. Liao, J.C.; Lu, Y.S. Calculation of active earth pressure on Rankine's theory. *Rock Soil Mech.* **2004**, *25*, 958–963.
48. Wang, Z.; Liu, X.; Wang, W. Calculation of nonlimit active earth pressure against rigid retaining wall rotating about base. *Appl. Sci.* **2022**, *12*, 9638. [CrossRef]
49. Zhang, C.; Chen, X.; Fan, W. Overturning stability of a rigid retaining wall for foundation pits in unsaturated soils. *Int. J. Geomech.* **2016**, *16*, 6015013. [CrossRef]
50. Xu, Y.; Dong, Y.; Jiang, Y.; Zhou, J.; Mao, Q. Influence of Parameter Variation of Saturated–Unsaturated Soil on Deformation and Stability of Foundation Pit. In Proceedings of the International Civil Engineering and Architecture Conference, Kyoto, Japan, 17–20 March 2023; pp. 721–731.
51. Ramakrishna Annapareddy, V.S.; Sufian, A.; Pain, A.; Scheuermann, A. A Generalised Framework to Estimate the Seismic Active Thrust on Rigid Retaining Walls with Partially Saturated Backfill. *Int. J. Geomech.* **2024**, *24*, 6024008. [CrossRef]
52. Yan, G.; Bore, T.; Schlaeger, S.; Scheuermann, A.; Li, L. Dynamic effects in soil water retention curves: An experimental exploration by full-scale soil column tests using spatial time-domain reflectometry and tensiometers. *Acta Geotech.* **2024**. [CrossRef]